Superradiance of optical phonons in two-dimensional materials

Guillaume Cassabois, G Fugallo, Bernard Gil

Letter

Superradiance of optical phonons in two-dimensional materials

G. Cassabois [1,*] G. Fugallo [2] and B. Gil [1]

[1] *Laboratoire Charles Coulomb, UMR 5221 CNRS, Université de Montpellier, 34095 Montpellier, France*

[2] *LTeN, UMR 6607 CNRS, Polytech Nantes, Université de Nantes, 44306 Nantes, France*

(Received 17 January 2022; revised 9 June 2022; accepted 22 July 2022; published 12 September 2022)

We study the superradiance of optical phonons during the two- to three-dimensional (2D-3D) crossover of the light-matter interaction in multilayers of atomic crystals. We show the emergence of a superradiant regime with a mode having a linewidth first increasing linearly with the number N of monolayers, and then decreasing as N^{-3} to zero because of the formation of stationary phonon polaritons. The linewidth culminates to values of the order of the longitudinal-transverse splitting. We estimate the extremum of the radiative efficiency for various 2D materials in the superradiant regime. We predict radiative efficiencies larger than 50% for optical phonons emitting between 6 and 165 μm. Superradiance appears as a key resource for mid- and far-infrared optophononics and advanced thermal management using multilayers of 2D materials as the active medium.

DOI: 10.1103/PhysRevResearch.4.L032040

Superradiance is the collective phenomenon where N identical elementary systems coherently radiate via a common light field with a spontaneous emission lifetime inversely proportional to N [1]. Initially demonstrated in atomic and molecular gases [2,3], superradiance was later observed in condensed matter, in the context of the excitonic emission in a large variety of systems [4–10]. In a recent paper [11], we discussed the analogy between excitons and optical phonons in the optical response of two-dimensional (2D) systems. We pointed out the existence of a finite spontaneous emission lifetime for 2D optical phonons, with a radiative efficiency as high as $\sim$10% in monolayers of hexagonal boron nitride (hBN) [11]. In contrast, in bulk hBN, the 3D optical phonons are in the strong-coupling regime with the electromagnetic field, leading to phonon polaritons that do not decay radiatively. Motivated by the flexibility of lamellar compounds to provide either monolayers or multilayers of atomic crystals [12], we address here the 2D-3D crossover of the light-matter interaction for optical phonons in superlattices of N identical monolayers.

We show the existence of superradiant optical phonons in multilayers of 2D materials. By taking the example of hBN, we study the emergence of a superradiant regime with a symmetric mode having a linewidth first increasing linearly with the number of monolayers, and then decreasing as N^{-3} to zero because of the formation of the stationary phonon-polariton states. The linewidth of the superradiant optical phonons culminates to values of the order of the longitudinal-transverse splitting in bulk hBN. We estimate the extremum of the radiative efficiency for various 2D materials in the superradiant regime. We predict radiative efficiencies larger than 50% for optical phonons with emission wavelengths between 6 and 165 μm.

In the following, we consider a superlattice of N hBN monolayers, that consists in a section of a bulk hBN crystal. The interlayer distance $b = 0.335$ nm is thus one-half of the c parameter in hBN [13]. Such a superlattice can be prepared by exfoliating a bulk hBN crystal, as for many layered compounds with weak van der Waals interlayer coupling [12]. According to the description of the hBN vibrational excitations in Ref. [14], there are two E_{1u} phonon modes in hBN, where the boron (B) atoms vibrate in phase inside the unit cell (Fig. 1, left), as the nitrogen (N) atoms do, but in opposite directions. These modes are degenerate strictly at $\mathbf{q} = \mathbf{0}$, and they split for $\mathbf{q} \neq \mathbf{0}$ giving rise to the E_{1u} longitudinal (LO) and E_{1u} transverse (TO) optical phonons. Since the microscopic B-N dipoles are the same from one basal plane to another, a macroscopic polarization builds up in the hBN crystal for the E_{1u} modes [14]. Their energies are the roots of the real part of the dielectric function, and their 30 meV splitting corresponds to the width of the reststrahlen band in bulk hBN [15]. The Raman-active E_{2g} mode is doubly degenerate with B atoms vibrating in opposite phase inside the unit cell (Fig. 1, right), as the N atoms. The electric dipoles in adjacent planes are of opposite sign and the resulting macroscopic polarization vanishes [14].

Dealing with the vibrational excitations of a N-layer section of a hBN crystal implies that the 2D optical phonons radiate in phase in N identical monolayers. This is a unique configuration in superradiance where the N elementary systems are often incoherently excited so that they first have to phase lock before a macroscopic coherence appears and produces a burst of emission [2–10]. Here, the van der Waals interaction between the atomic layers guarantees the phase relation between the atomic vibrations in adjacent basal planes, and hence the coherent radiative interaction of the E_{1u} optical phonons in the hBN superlattice.

*guillaume.cassabois@umontpellier.fr

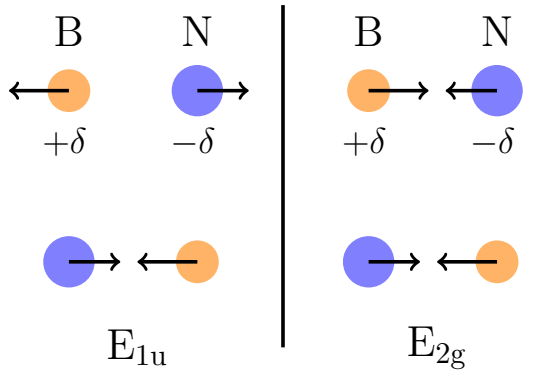

FIG. 1. Atomic displacements inside the unit cell of hBN for the E_{1u} and E_{2g} optical phonons at $\mathbf{q} = \mathbf{0}$. The c axis is perpendicular to the in-plane displacements (arrows). The top B and N atoms are in a different atomic layer than the bottom ones. $\delta > 0$ characterizes the electronegativity.

We describe the optophononic properties of our superlattice in the framework of a semiclassical model based on a transfer matrix approach, in analogy to 2D excitons in a superlattice of quantum wells [16]. Other frameworks have been developed for the treatment of the exciton-polariton crossover [17–19]. Since the microscopic dipoles are in phase in adjacent layers for the E_{1u} modes (Fig. 1, left), the transfer matrix of the superlattice is $(MP)^N$, where M and P describe the monolayer and the interlayer spacer, respectively (see Appendix A), $N = e/b$ with e the thickness of the multilayer hBN slab, and $b = 0.335$ nm is the spacer thickness.

Taking a radiative linewidth $\gamma_r = 0.2$ meV and a total linewidth $\Gamma = 2$ meV according to Ref. [11], and a spacer dielectric constant $\epsilon_\infty = 4.95$ from Ref. [20], and without any fitting parameter, the limit $N \gg 1$ leads to a reflectivity spectrum with a stop band, the so-called reststrahlen band, of width much larger than the 30 meV in bulk hBN [15]. This inconsistency is due to the fact that, in this first model, the interaction between the hBN monolayers only stems from the radiative coupling. Whereas this assumption is relevant for excitons localized in quantum wells [16], it is no longer valid for phonons because of the interlayer coupling by the van der Waals interaction. We thus introduce a renormalization factor f for the refractive index of the background medium where the superlattice of hBN monolayers is embedded. In our modified transfer matrix model, the renormalized refractive index writes $f\sqrt{\epsilon_\infty}$. In order to maintain the optical thickness $\sqrt{\epsilon_\infty}e$ invariant for the multilayer hBN slab, one has in turn to consider an effective number of monolayers $\widetilde{N}$. Taking $\widetilde{N} = N/f$ leads to the correct optical thickness $f\sqrt{\epsilon_\infty}\widetilde{N}b = \sqrt{\epsilon_\infty}e$. In the following, the optophononic properties of multilayer hBN of thickness e are derived from the transfer matrix $(MP)^{\widetilde{N}}$, with the renormalization factor f as the only adjustable parameter.

We compare our calculations to the thickness-dependent reflectivity spectra available in the Supplemental Material of Ref. [21]. The renormalization factor f is adjusted to reach the longitudinal-transverse splitting Δ_{LT} in hBN, i.e., the energy splitting between the LO and TO phonons (dashed and dotted lines in Fig. 2, respectively), which determines the width of the reflectivity reststrahlen band. Taking $f = 8.8$ leads to the well-documented value $\Delta_{LT} = 30$ meV in hBN [15]. It also fairly reproduces the reflectivity spectrum of the thickest hBN slab ($e = 6400$ nm, violet line in Fig. 2). Our model not only accounts for the smooth transition from a Lorentzian profile at low hBN thickness to the textbook reststrahlen band in the bulk limit, but also for the gradual increase of the reflectivity maximum as a function of the hBN thickness (Fig. 2). This contrasts with a classical model based on a local dielectric function $\epsilon(\omega)$, for which the reflectivity maximum is already higher than 90% for the thinnest hBN slab ($e = 60$ nm, see Appendix B). The remaining discrepancy between experiment and theory at low hBN thickness in Fig. 2 is attributed to the possible existence of different multilayer segments, the total thickness of which is measured by atomic force microscopy [21], but only the top one is probed by reflectivity. The smooth buildup of the reflectivity reststrahlen band results from the emergence of superradiance for optical phonons in the hBN superlattice. Our semiclassical model allows detailed insight into the superradiant optical phonons at low $\widetilde{N}$ number, as discussed below.

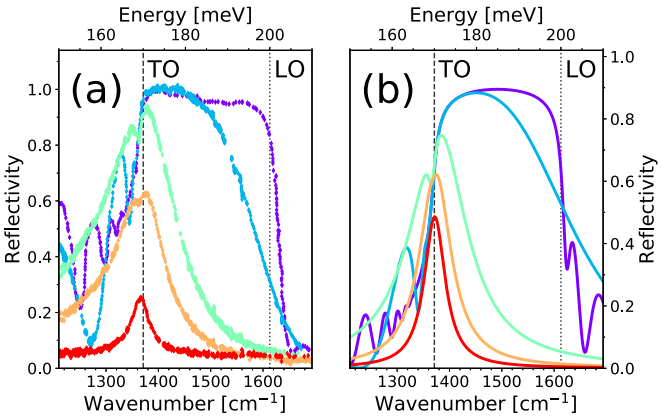

FIG. 2. Buildup of the reflectivity reststrahlen band as a function of the hBN thickness. (a) Experimental data for hBN thicknesses $e = 60$ (red), 105 (orange), 210 (green), 1020 (blue), and 6400 nm (violet), adapted from the Supplemental Material of Ref. [21]. (b) Semiclassical calculations with a transfer matrix approach for a superlattice of $\widetilde{N}$ hBN monolayers ($\widetilde{N} = e/bf$ with $f = 8.8$).

The reflectivity spectrum is displayed in Fig. 3(a) for $1 \leqslant \widetilde{N} < 20$. In the case $\widetilde{N} = 1$, the reflectivity contrast C_1 is given by the 2D limit $(\gamma_r/\Gamma)^2$, as initially pointed out for excitons in semiconductor quantum wells [22]. With $\gamma_r = 0.2$ meV and $\Gamma = 2$ meV [11], $C_1 = 10^{-2}$, consistently with the violet reflectivity spectrum in Fig. 3(a). The reflectivity contrast has thus an upper bound given by the square of the radiative efficiency η^2, where $\eta = \gamma_r/(\gamma_r + \gamma_{nr})$ with $\gamma_r + \gamma_{nr} \leqslant \Gamma$ because of pure dephasing processes. The increase of the reflectivity contrast $C_{\widetilde{N}}$ with the effective number of monolayers in Fig. 3(a) is a direct signature for higher radiative efficiencies in thicker hBN superlattices. Since the nonradiative linewidth γ_{nr} is determined by anharmonic processes that hardly depend on the hBN thickness [11,23], this indicates that the radiative linewidth increases with $\widetilde{N}$. This effect is also observable in Fig. 3(a) from the broadening of the Lorentzian reflectivity line as a function of $\widetilde{N}$.

For a given multilayer stack of $\widetilde{N}$ monolayers, there are in fact $\widetilde{N}$ modes of the coupled photon-phonon system. Only one

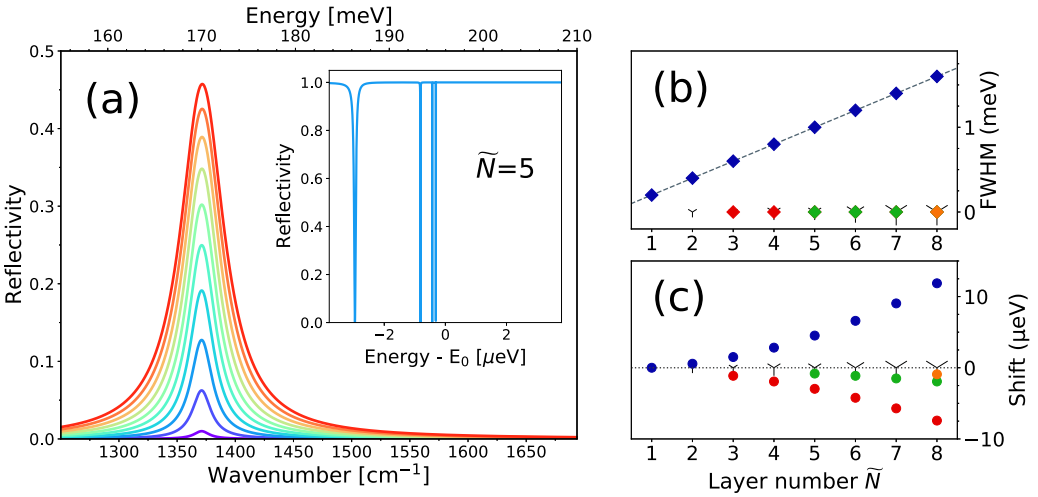

FIG. 3. (a) Reflectivity spectrum of a hBN multilayer stack at low $\widetilde{N}$ ($1 \leqslant \widetilde{N} < 20$) for $\gamma_r/\Gamma = 0.1$. Inset: Zoom around E_0 of the reflectivity spectrum at $\widetilde{N} = 5$ for $\gamma_r/\Gamma = 1$. (b) Imaginary and (c) real parts of the poles of the transmission of the hBN multilayer stack as a function of $\widetilde{N}$ for $\gamma_r/\Gamma = 1$. Tristars correspond to the transmission poles beyond our numerical precision, with a size proportional to their degeneracy. The dashed line in (b) is the linear function $\widetilde{N}\gamma_r$. For all calculations, $\gamma_r = 0.2$ meV.

of these $\widetilde{N}$ modes is observed in Fig. 3(a). This comes from the low value of the γ_r/Γ ratio ($\gamma_r/\Gamma = 0.1$), blurring the other $\widetilde{N} - 1$ ultranarrow resonances related to almost dark modes of the coupled photon-phonon system. In order to resolve these subradiant modes, one needs to perform the reflectivity calculations for $\gamma_r/\Gamma = 1$. An example is given in the inset of Fig. 3(a) for $\widetilde{N} = 5$, where the reflectivity spectrum is considerably zoomed in a spectral window of few μeV (∼few 10^{-2} cm^{-1}) around the phonon energy E_0. The expected four resonances are resolved, and they are all redshifted with sub-μeV linewidths. Such ultranarrow lines result from the negligible interaction with the transverse electromagnetic field freely propagating outside the multilayer stack. These subradiant modes are the precursors of the phonon-polariton states developing for $\widetilde{N} \gg 1$, with a lower polaritonic branch characterized by a large density of states just below the bare phonon energy E_0.

The complex energies of the $\widetilde{N}$ coupled photon-phonon modes can be calculated from the poles of the transmission of the whole multilayer stack [16]. Figures 3(b) and 3(c) display the imaginary and real parts of the complex energies, respectively, for $1 \leqslant \widetilde{N} \leqslant 8$. When the poles are beyond our numerical precision, the values are plotted as tristars with a size proportional to their degeneracy. When $\widetilde{N}$ increases, one follows the apparition of more and more subradiant modes with a negative energy shift [Fig. 3(c)], and a width much smaller than γ_r [Fig. 3(b)]. In contrast, one mode has a width increasing as $\widetilde{N}\gamma_r$ [dashed line in Fig. 3(b)], i.e., the genuine fingerprint of superradiance for optical phonons. We point out that phonon superradiance was previously discussed, but for other types of cooperative effects involving phonons [24,25]. Although the shift is much smaller than γ_r for small $\widetilde{N}$, it scales quadratically with $\widetilde{N}$ [Fig. 3(c)], and it eventually surpasses the linewidth for larger values of $\widetilde{N}$, as detailed below (Fig. 4). Nevertheless, in thin hBN superlattices, the reflectivity contrast $C_{\widetilde{N}}$ is determined by the superradiant mode, so that a fair approximation of $C_{\widetilde{N}}$ at low $\widetilde{N}$ is given by the expression $C_{\widetilde{N}} \sim (\frac{\widetilde{N}\gamma_r}{\widetilde{N}\gamma_r+(\Gamma-\gamma_r)})^2 \sim (\frac{\widetilde{N}\eta}{(\widetilde{N}-1)\eta+1})^2$. For $\eta = 0.1$, one gets $C_9 \sim 0.25$ and $C_{19} \sim 0.45$, consistently with Fig. 3(a).

While the linewidth of the symmetric mode first increases linearly with $\widetilde{N}$ in the regime of superradiance, it then saturates and decreases as $\widetilde{N}^{-3}$ for $\widetilde{N} \gg 1$, as shown in Fig. 4 where the complex energy of only this mode is displayed (circles and diamonds for the real and imaginary parts, respectively). When the multilayer stack is thick enough in comparison to $\lambda_0/2\sqrt{\epsilon_\infty}$ (shaded area limit in Fig. 4), propagation effects allow a reversible energy exchange between photons and phonons, and phonon polaritons build up

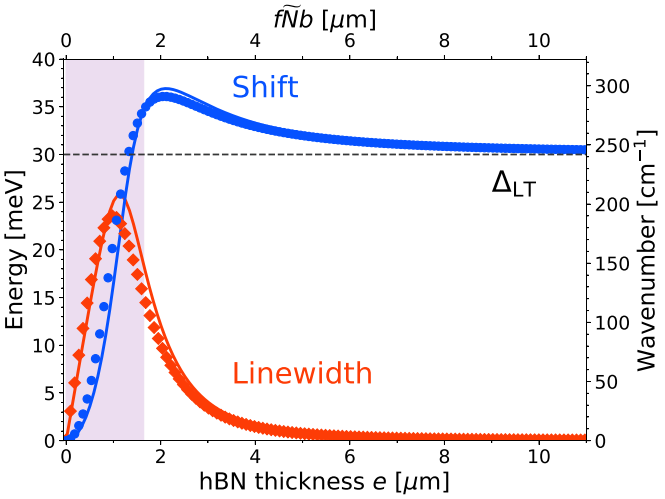

FIG. 4. Half width at half maximum (HWHM) and shift of the symmetric mode of the coupled phonon-photon system during the 2D-3D crossover. Solid lines: Classical calculations using a local dielectric function for describing light propagation in a multilayer hBN slab of thickness e. Symbols: Semiclassical calculations using the generalized transfer matrix approach for a periodic array of $\widetilde{N}$ monolayers with an interlayer spacing b as a function of $f\widetilde{N}b$. $\Delta_{LT} = 30$ meV is the longitudinal-transverse splitting in bulk hBN. Shaded area: $e \leqslant \lambda_0/2\sqrt{\epsilon_\infty}$, with $\lambda_0 = hc/E_0$.

during the crossover to the strong-coupling regime in 3D [11]. Since polaritons are the eigenstates of the coupled photon-phonon system in 3D, the linewidths of all $\widetilde{N}$ modes vanish when $\widetilde{N} \gg 1$. Remarkably, the energy shift saturates and converges to an asymptotic value given by the longitudinal-transverse splitting Δ_{LT} (dashed line in Fig. 4).

In order to accurately determine the optimal thickness of the maximal linewidth and to test the robustness of our approach with respect to the introduction of the renormalization factor f, we implement a second method of calculations. As shown by Andreani in the excitonic case of the 2D-3D crossover and the buildup of exciton polaritons [16], the complex energy of the symmetric mode can be alternatively calculated in a classical framework by finding the complex root of the equation [16,26],

$$\sqrt{\frac{\epsilon(\omega)}{\epsilon_\infty}}\tan\left(\sqrt{\epsilon(\omega)}\,\frac{\omega e}{2c}\right) = i, \tag{1}$$

where $\epsilon(\omega) = \epsilon_\infty[1 + \Delta_{\mathrm{LT}}/(E_0 - \hbar\omega)]$ is here the local dielectric function of the hBN slab in the limit of negligible damping. The results are displayed as solid lines in Fig. 4. The calculations are basically identical within the semiclassical and classical frameworks. Both models predict values of the maximal linewidth and maximal shift differing by less than 10%, and the asymptotic limit is exactly Δ_{LT} in the two cases. We note they also coincide on the thickness giving the maximal linewidth, i.e., $e \sim 1.1\ \mu$m in the classical model and $f\widetilde{N}b \sim 0.99\ \mu$m in the semiclassical one based on the transfer matrix approach. This optimal thickness is slightly below $\lambda_0/2\sqrt{\epsilon_\infty}$ of the order of 1.6 μm in hBN.

A key point in Fig. 4 is the fact that the half width at half maximum (HWHM) has an extremum of order Δ_{LT}. This effect is not specific to hBN, and it is a generic result that does not depend on the parameters of the materials, as checked for different Δ_{LT}, E_0, and ϵ_∞. Therefore the radiative efficiency η_m at maximal superradiance can be easily estimated for other materials from

$$\eta_m \sim \frac{2\Delta_{\mathrm{LT}}}{2\Delta_{\mathrm{LT}} + \Gamma_{\mathrm{Raman}}}, \tag{2}$$

where the width of the Raman line Γ_{Raman} is assumed to provide a fair estimate for the nonradiative linewidth γ_{nr}.

In Table I we list a few lamellar compounds by decreasing Δ_{LT}. These crystals belong to well-known families that are actively studied in 2D materials research, such as mono- and dichalcogenides of transition metals, and 2D halides. The larger the Born effective charge, the wider the reststrahlen band, so that an ionic crystal such as ZrS_2 has much larger Δ_{LT} than MoS_2 with a quasicovalent bonding [27]. Boron and nitrogen being light elements, the reststrahlen band reaches particularly high values in hBN. We note the absence of a monotonous dependence of the phonon energy E_0 with Δ_{LT}. However, the selected 2D materials in Table I span almost continuously a wide spectral range in the mid- and far-infrared domains (see the λ column in Table I). The Raman linewidth barely varies from one material to another, with values of a few to tens of cm^{-1}, i.e., in the meV range. This originates from the highly efficient anharmonic decay of optical phonons on a timescale of typically 1 ps in a large variety of crystals [33,34]. Using Eq. (2) we estimate the radiative efficiency at maximal superradiance η_m. We predict extremely high values (Table I). While the radiative linewidth γ_r of 2D optical phonons is always a fraction of γ_{nr} resulting in low radiative efficiencies in monolayers (with the exception of hBN where $\eta \sim 10\%$ [11]), superradiance in superlattices of monolayers allows us to reach η_m of order unity for all 2D materials (Table I). This phenomenology contrasts with the one of 2D excitons, where the radiative efficiency can take large values in single quantum wells and atomically thin crystals, provided the sample quality is high enough. Here, the cooperative coherent coupling of 2D optical phonons is the key for achieving high radiative yields, opening the avenue of optophonics in multilayers of atomic crystals, with fascinating fundamental properties to explore and applications in infrared emission and advanced thermal management.

TABLE I. Comparison of various 2D materials: longitudinal-transverse splitting Δ_{LT}, Raman linewidth Γ_{Raman}, estimated radiative efficiency at maximal superradiance η_m, and emission wavelength range λ.

2D material	Δ_{LT} (cm^{-1})		Γ_{Raman} (cm^{-1})		η_m	λ (μm)
hBN	242	[20]	8	[23]	0.98	6.3–7.3
ZrS_2	170	[27]	20	[28]	0.95	28–55
CdI_2	75	[27]	4	[29]	0.97	75–165
GaSe	40	[30]	8	[31]	0.91	39–47
MoS_2	3	[27]	5	[32]	0.5	25.8–26

We have addressed the 2D-3D crossover of the light-matter interaction for optical phonons in superlattices of atomic crystals. We have shown the emergence of superradiance with a symmetric mode of the photon-phonon system having a linewidth increasing linearly with the number of monolayers. In the 3D limit of bulk crystals, this linewidth vanishes because of the formation of the stationary phonon-polariton states. We have estimated the extremum of the radiative efficiency at maximal superradiance for various lamellar compounds actively studied in 2D materials research. We predict radiative efficiencies of order unity for optical phonons emitting in the mid- and far-infrared domains, at wavelengths between 6 and 165 μm. Superradiance appears as a key resource for this field of optophononics and advanced thermal management using multilayers of 2D materials as the active medium.

We gratefully acknowledge V. Jacques, A. Rousseau, and P. Valvin for critical reading, and G. Bastard and J. M. Gérard for discussion. This work was financially supported by the BONASPES Project No. (ANR-19-CE30-0007), the NAPOLI Project No. (ANR-18-CE24-0022), the ZEOLIGHT Project No. (ANR-19-CE08-0016), and the CHROMIC Project No. (PdL- N°2018-12126).

APPENDIX A: TRANSFER MATRIX APPROACH

The transfer matrix connecting the electric fields on the left and right sides of a 2D monolayer is [11]

$$M = \frac{1}{t}\begin{pmatrix} 1 & -r \\ r & 1+2r \end{pmatrix}, \tag{A1}$$

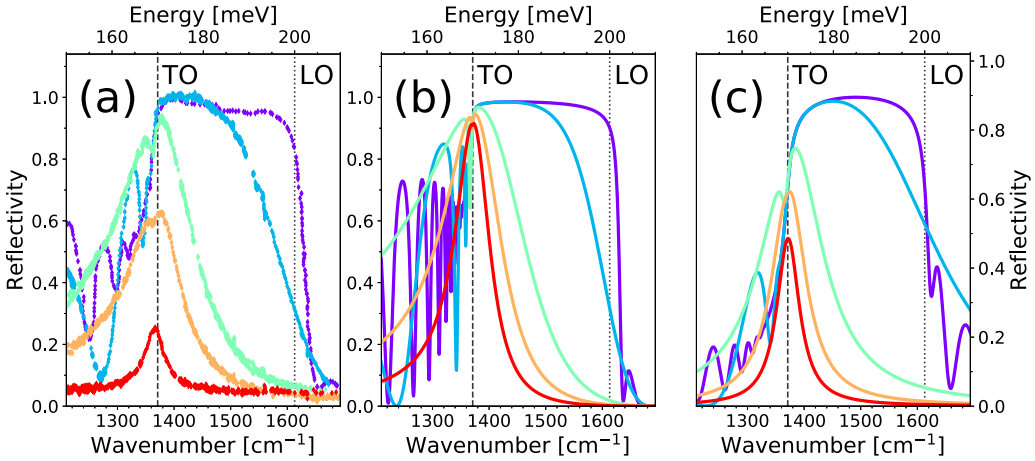

FIG. 5. (a) Experimental reflectivity data for hBN thicknesses $e = 60$ (red), 105 (orange), 210 (green), 1020 (blue), and 6400 nm (violet), adapted from the Supplemental Material of Ref. [21]. (b) Classical calculations for a hBN slab of thickness e with the local dielectric function determined in Ref. [20]. (c) Semiclassical calculations with a transfer matrix approach for a superlattice of $\widetilde{N}$ hBN monolayers ($\widetilde{N} = e/bf$ with $f = 8.8$).

with $t = 1 + r$, where r is the reflectivity amplitude of a 2D monolayer given by

$$r = \frac{i\frac{\gamma_r}{2}}{E_0 - \hbar\omega - i\frac{\Gamma}{2}}, \tag{A2}$$

with E_0 the phonon energy, γ_r the radiative linewidth given by $\frac{\hbar}{T_1}$ with T_1 the spontaneous emission lifetime, and Γ the total linewidth given by $\frac{2\hbar}{T_2}$ with T_2 the decoherence time.

Propagation inside a medium of complex refractive index $\sqrt{\epsilon_\infty}$ and thickness b is characterized by the diagonal matrix P,

$$P = \begin{pmatrix} e^{i\phi} & 0 \\ 0 & 1/e^{i\phi} \end{pmatrix}, \tag{A3}$$

where $\phi = -\sqrt{\epsilon_\infty}\omega b/c$ is the complex dephasing.

APPENDIX B: REFLECTIVITY CALCULATIONS

In this Appendix, we compare the reflectivity spectra calculated with two methods: (1) the semiclassical model of the generalized transfer matrix approach used in the core of the text [Fig. 5(c)], and (2) the classical model of the local linear response for the dielectric function given in Ref. [20] [Fig. 5(b)].

While the semiclassical model accounts for the gradual increase of the reflectivity maximum as a function of the hBN thickness, the classical model leads to a reflectivity maximum already higher than 90% for the thinnest hBN slab ($e = 60$ nm). As explained in the main text, the semiclassical model allows a detailed insight into the emergence of superradiant optical phonons.

[1] R. H. Dicke, Coherence in spontaneous radiation processes, Phys. Rev. **93**, 99 (1954).

[2] N. Skribanowitz, I. P. Herman, J. C. MacGillivray, and M. S. Feld, Observation of Dicke Superradiance in Optically Pumped HF Gas, Phys. Rev. Lett. **30**, 309 (1973).

[3] M. Gross, C. Fabre, P. Pillet, and S. Haroche, Observation of Near-Infrared Dicke Superradiance on Cascading Transitions in Atomic Sodium, Phys. Rev. Lett. **36**, 1035 (1976).

[4] M. Orrit and P. Kottis, Surface and bulk spectroscopy of a molecular crystal: Effect of relaxation and thermal or static disorder, in *Advances in Chemical Physics* (Wiley, New York, 1988), pp. 1–253.

[5] T. Itoh, M. Furumiya, T. Ikehara, and C. Gourdon, Size-dependent radiative decay time of confined excitons in CuCl microcrystals, Solid State Commun. **73**, 271 (1990).

[6] H. Fidder, J. Knoester, and D. A. Wiersma, Superradiant emission and optical dephasing in J-aggregates, Chem. Phys. Lett. **171**, 529 (1990).

[7] M. Hübner, J. P. Prineas, C. Ell, P. Brick, E. S. Lee, G. Khitrova, H. M. Gibbs, and S. W. Koch, Optical Lattices Achieved by Excitons in Periodic Quantum Well Structures, Phys. Rev. Lett. **83**, 2841 (1999).

[8] M. Scheibner, T. Schmidt, L. Worschech, A. Forchel, G. Bacher, T. Passow, and D. Hommel, Superradiance of quantum dots, Nat. Phys. **3**, 106 (2007).

[9] G. T. Noe II, J.-H. Kim, J. Lee, Y. Wang, A. K. Wójcik, S. A. McGill, D. H. Reitze, A. A. Belyanin, and J. Kono, Giant superfluorescent bursts from a semiconductor magneto-plasma, Nat. Phys. **8**, 219 (2012).

[10] G. Rainò, M. A. Becker, M. I. Bodnarchuk, R. F. Mahrt, M. V. Kovalenko, and T. Stöferle, Superfluorescence from lead halide perovskite quantum dot superlattices, Nature (London) **563**, 671 (2018).

[11] G. Cassabois, G. Fugallo, C. Elias, P. Valvin, A. Rousseau, B. Gil, A. Summerfield, C. J. Mellor, T. S. Cheng, L. Eaves, C. T. Foxon, P. H. Beton, M. Lazzeri, A. Segura, and S. Novikov, Exciton and Phonon Radiative Linewidths in Monolayer Boron Nitride, Phys. Rev. X **12**, 011057 (2022).

[12] A. K. Geim and I. V. Grigorieva, Van der Waals heterostructures, Nature (London) **499**, 419 (2013).

[13] R. S. Pease, An x-ray study of boron nitride, Acta Crystallogr. **5**, 356 (1952).

[14] K. Michel and B. Verberck, Phonon dispersions and piezoelectricity in bulk and multilayers of hexagonal boron nitride, Phys. Rev. B **83**, 115328 (2011).

[15] J. Caldwell, I. Aharonovich, G. Cassabois, J. H. Edgar, B. Gil, and D. N. Basov, Photonics with hexagonal boron nitride, Nat. Rev. Mater. **4**, 552 (2019).

[16] L. C. Andreani, Polaritons in multiple quantum wells, Phys. Status Solidi B **188**, 29 (1995).

[17] G. Björk, S. Pau, J. M. Jacobson, H. Cao, and Y. Yamamoto, Excitonic superradiance to exciton-polariton crossover and the pole approximations, Phys. Rev. B **52**, 17310 (1995).

[18] M. Bamba and H. Ishihara, Crossover of exciton-photon coupled modes in a finite system, Phys. Rev. B **80**, 125319 (2009).

[19] M. Ichimiya, M. Ashida, H. Yasuda, H. Ishihara, and T. Itoh, Observation of Superradiance by Nonlocal Wave Coupling of Light and Excitons in CuCl Thin Films, Phys. Rev. Lett. **103**, 257401 (2009).

[20] A. Segura, L. Artús, R. Cuscó, T. Taniguchi, G. Cassabois, and B. Gil, Natural optical anisotropy of h-BN: Highest giant birefringence in a bulk crystal through the mid-infrared to ultraviolet range, Phys. Rev. Materials **2**, 024001 (2018).

[21] J. D. Caldwell, A. V. Kretinin, Y. Chen, V. Giannini, M. M. Fogler, Y. Francescato, C. T. Ellis, J. G. Tischler, C. R. Woods, A. J. Giles, M. Hong, K. Watanabe, T. Taniguchi, S. A. Maier, and K. S. Novoselov, Sub-diffractional volume-confined polaritons in the natural hyperbolic material hexagonal boron nitride, Nat. Commun. **5**, 5221 (2014).

[22] L. C. Andreani, F. Tassone, and F. Bassani, Radiative lifetime of free excitons in quantum wells, Solid State Commun. **77**, 641 (1991).

[23] R. Cuscó, B. Gil, G. Cassabois, and L. Artús, Temperature dependence of Raman-active phonons and anharmonic interactions in layered hexagonal BN, Phys. Rev. B **94**, 155435 (2016).

[24] E. M. Chudnovsky and D. A. Garanin, Phonon Superradiance and Phonon Laser Effect in Nanomagnets, Phys. Rev. Lett. **93**, 257205 (2004).

[25] Y.-J. Jiang, H. Lü, and H. Jing, Superradiance-driven phonon laser, Chin. Phys. Lett. **35**, 044205 (2018).

[26] K. L. Kliewer and R. Fuchs, Optical Modes of Vibration in an Ionic Crystal Slab Including Retardation. II. Radiative Region, Phys. Rev. **150**, 573 (1966).

[27] G. Lucovsky, R. M. White, J. A. Benda, and J. F. Revelli, Infrared-reflectance spectra of layered group-IV and group-VI transition-metal dichalcogenides, Phys. Rev. B **7**, 3859 (1973).

[28] S. Mañas-Valero, V. García-López, A. Cantarero, and M. Galbiati, Raman spectra of ZrS_2 and $ZrSe_2$ from bulk to atomically thin layers, Applied Sciences **6**, 264 (2016).

[29] A. Anderson and Y. W. Lo, Raman and infrared spectra of crystals with the cadmium iodide structure, Spectrosc. Lett. **14**, 603 (1981).

[30] T. J. Wieting and J. L. Verble, Interlayer bonding and the lattice vibrations of β-GaSe, Phys. Rev. B **5**, 1473 (1972).

[31] M. R. Molas, A. V. Tyurnina, V. Zólyomi, A. K. Ott, D. J. Terry, M. J. Hamer, C. Yelgel, A. Babiński, A. G. Nasibulin, A. C. Ferrari, V. I. Fal'ko, and R. Gorbachev, Raman spectroscopy of GaSe and InSe post-transition metal chalcogenides layers, Faraday Discuss. **227**, 163 (2021).

[32] H. Li, Q. Zhang, C. C. R. Yap, B. K. Tay, T. H. T. Edwin, A. Olivier, and D. Baillargeat, From bulk to monolayer MoS_2: Evolution of Raman scattering, Adv. Funct. Mater. **22**, 1385 (2012).

[33] F. Vallée and F. Bogani, Coherent time-resolved investigation of LO-phonon dynamics in GaAs, Phys. Rev. B **43**, 12049 (1991).

[34] T. Kang, J. Zhang, A. Kundu, K. Reimann, M. Woerner, T. Elsaesser, B. Gil, G. Cassabois, C. Flytzanis, G. Fugallo, M. Lazzeri, R. Page, and D. Jena, Ultrafast nonlinear phonon response of few-layer hexagonal boron nitride, Phys. Rev. B **104**, L140302 (2021).